Editors' Suggestion

# High-resolution acoustic field mapping of gigahertz phononic crystals with atomic force microscopy

Alessandro Pitanti,[1,2,3,*] Mingyun Yuan,[1] Simone Zanotto,[3] and Paulo Ventura Santos[1]

[1] *Paul-Drude-Institut für Festkörperelektronik, Leibniz-Institut im Forschungsverbund Berlin e.V., 5-7 Hausvogteiplatz, Berlin 10117, Germany*

[2] *Dipartimento di Fisica "E. Fermi", Università di Pisa, Largo B. Pontecorvo 3, Pisa 56127, Italy*

[3] *NEST, CNR Istituto Nanoscienze and Scuola Normale Superiore, piazza San Silvestro 12, Pisa 56127, Italy*

(Received 18 July 2023; revised 25 September 2023; accepted 2 November 2023; published 27 November 2023)

On-chip technology based on acoustic waves is a strong asset in modern telecommunications, with the prospects of becoming a cornerstone of next-generation devices. In this context, mapping and manipulating acoustic waves through coherent scattering is pivotal for a nontrivial control of the flow of acoustic energy, which could consequently enable advanced information manipulation. To this end, here a technique for mapping acoustic fields is introduced and used for characterizing micrometric-sized phononic crystals defined in GaAs slabs and excited by gigahertz surface acoustic waves based on atomic force microscopy. It is shown that incoherent scattering excites a wide distribution of modes, which enables the mapping of the dispersion relation of the two-dimensional structures, while the phononic crystal symmetry directly correlates with coherent scattering effects. Enabling the use of acoustic atomic force microscopy and understanding the role of scattering are of paramount importance for the versatile use of gigahertz acoustic waves in technological applications, setting the baseline for advanced operations like hyperspectral filtering, beam steering, or spatial-division multiplexing.

DOI: 10.1103/PhysRevApplied.20.054054

## I. INTRODUCTION

The last decades have witnessed a rich activity toward the integration of acoustic technologies within electrical circuits in high-frequency hybrid devices. The main role in this trend has been played by surface acoustic waves (SAWs) [1], which are waves propagating along a surface that can be easily introduced in several material platforms exploiting the piezoelectric effect [2]. Given their high operation frequency (typically up to $\sim$ 10 GHz) and quality factors, simple, one-dimensional SAW delay-line resonators have found wide application as sensors [3,4], spectral filters [5], and oscillators [6] for telecommunication applications [7]. Further technological advances have made SAWs a flexible tool for both applied and fundamental physics, the latter reaching, for example, the quantum regime and enabling single-particle manipulation [8].

In this wide scenario, SAW-based technologies offer novel tools for manipulating information-carrying waves on-chip. Increasing the degree of freedom in the control of SAWs can thus be a relevant key for the transition to sixth-generation (6G) technologies: one can imagine, along with an increase in operating frequency, an enhancement of the data transmission rate through wave manipulation with complex spatial or frequency multiplexing, allowing simultaneous on-chip operations, such as filtering, on several communication channels.

As for electromagnetic waves, acoustic waves can be manipulated by using artificially defined structures in the form of phononic crystals (PCs) or acoustic metasurfaces. The impressive results obtained in advanced light control are presently being translated to acoustic waves with micron-sized wavelengths (approximately gigahertz frequencies), propagating on the millimeter-to-centimeter scale. Interesting proof-of-concept experiments have already been demonstrated or theoretically proposed, including acoustic holography [9], negative acoustic refraction [10], as well as several topological effects [11–13], albeit most in the kilohertz to megahertz frequency range, with only a few exceptions reaching the hundreds of megahertz [14,15] and gigahertz [16] ranges. The latter frequency ranges are the most promising for integration with modern communication technologies, since they offer devices with millimeter-to-centimeter footprints operating at the frequency of the standard electromagnetic carrier waves for wireless telecommunications. Moreover, the acoustic wavelengths of the most-used semiconductor materials in the gigahertz range are comparable to those of third-telecom-window photons.

*alessandro.pitanti@nano.cnr.it

 

SAW-based structures thus offer a powerful platform for photon manipulation [17] and optomechanical hybrid systems for light-based telecommunications and favour interesting features such as coherent wavelength conversion [18–20]. The development of high-frequency phononic crystals requires efficient techniques for probing gigahertz acoustic field distributions in the submicron length scale. Most of these acoustic devices are routinely measured using either integrated probes [21,22] or techniques based on light, including interferometry [23–26] and Brillouin scattering. While presenting several advantages, the former case does not allow for direct mapping of the vibrational field, while the latter presents intrinsic limitations associated with the finite spatial resolution imposed by the light diffraction limit. Moreover, interferometry shows a lack of sensitivity to in-plane fields, whereas Brillouin spectroscopy, while giving access to the mode dispersion, can hardly be used for spatial mapping, due to the necessity of multiscanning within a surface at several angles of incidence [27,28].

A powerful tool for mapping vibrational fields, which so far has only been scarcely used, is atomic acoustic force microscopy (AAFM), a variation of conventional atomic force microscopy (AFM). This fast-scanning technique was initially introduced for field mapping of kilohertz to megahertz elastic wave structures [29] and subsequently extended to gigahertz SAWs [30–34]. The subnanometer lateral sensitivity of AAFM makes it a natural candidate for field mapping of complex phononic devices operating at submicron acoustic wavelengths and frequencies in the range of tens to hundreds of gigahertz. To the best of our knowledge, however, AAFM has so far never been applied for investigating gigahertz modes in PC devices.

In this paper, we introduce AAFM as a powerful high-resolution tool for mapping submicron fields in gigahertz PCs. In particular, we report on an AAFM investigation of PCs with different symmetries operating at around 1 GHz. We show that AAFM allows for recording, at a fine level of detail, the acoustic field distribution within micron-sized PCs, which are already among the smallest features that can be resolved using visible-light-based interferometry. Using the mapping features of AAFM, we analyze isofrequency contours in reciprocal space, estimating and differentiating between acoustic scattering channels induced by the PC structure and those originating from pervasive imperfections, the former being ultimately responsible for deterministic wave manipulation.

The paper is organized as follows. After a brief introduction to the device fabrication and theoretical design, we introduce our characterization bench based on AFM. An initial investigation of the SAW on the top surface of the semiconductor substrate is followed by the evaluation and characterization of the mechanical Bloch modes within the suspended phononic crystal membranes.

## II. DEVICE DESIGN AND EXPERIMENTAL SETUP

We designed a set of devices defined by a square lattice of holes within a suspended 220-nm-thick GaAs slab. The choice of GaAs as device layer considers its natural piezoelectricity [35] and compatibility with nanomachining. Moreover, similar platforms have shown optimal performance in photonic [36] and hybrid optomechanical [37] devices. The lattice constant of the devices' periodic pattern was chosen to be $a = 1.125$ μm, while two different kinds of holes were considered: square holes with sides $l = 0.47a$ [$S_{PC}$, see Fig. 1(a)] and rectangular holes with sides $l_x = 0.7a$ and $l_y = 0.32a$ [$R_{PC}$, see Fig. 1(b)], respectively. The different hole geometries translate into a remarkably different aspect in their simulated phononic band structures. The simulations have been performed using a commercial finite-element method (FEM) solver, more details of which can be found in Ref. [16]. As expected, the band

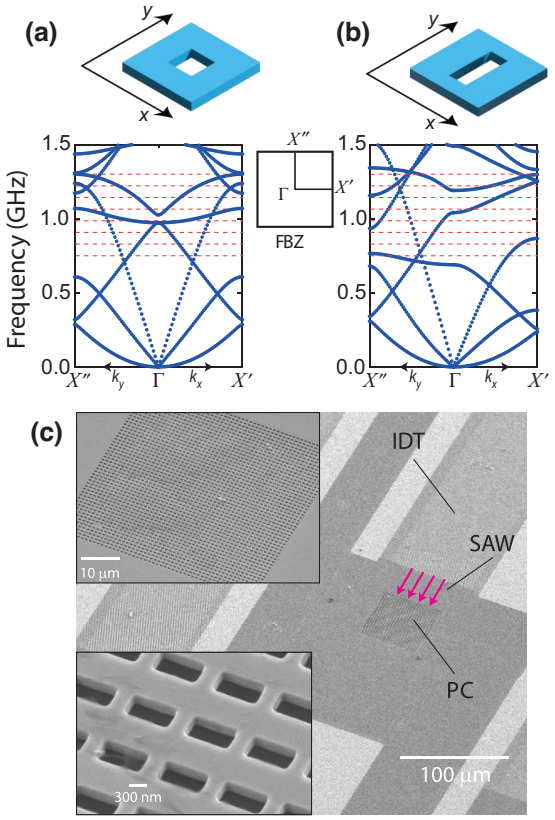


FIG. 1. (a),(b) Sketches of the unit cell and simulated phononic band structure for the in-plane infinite PCs consisting of (a) square ($S_{PC}$) and (b) rectangular ($R_{PC}$) holes etched in a 220-nm-thick GaAs membrane. The horizontal dashed lines indicate the resonant frequencies of the interdigital transducers for surface acoustic waves used to excite the PCs. (c) Scanning electron micrograph of one of the investigated devices. The full released membrane and an enlarged view of a few lattice periods are shown in the insets.

structure of the $R_{PC}$ shows an asymmetric dispersion along the high-symmetry paths in the first Brillouin zone (FBZ), $\Gamma \rightarrow X' \equiv (\pi/a, 0)$ and $\Gamma \rightarrow X'' \equiv (0, \pi/a)$ [see inset in Fig. 1(a),(b)], whereas the $S_{PC}$ bands are symmetric along the same paths.

The lowest mechanical band in Figs. 1(a) and 1(b), characterized by a typical parabolic dispersion, is ultimately responsible for the effective parameters of the low-frequency *drum* modes, which are determined by the patterned region shape and size and are characterized by strong out-of-plane displacements. An effect of the asymmetric patterning is already present in these low-frequency modes, which are well within the metasurface regime (i.e., with all structural length scales smaller than the acoustic wavelength [38]). Conversely, here we investigate the role of asymmetry in the phononic crystal regime, where the structural length scales are comparable to the acoustic wavelength.

To perform a spectroscopic analysis of the PC devices, we included eight kinds of interdigitated transducers (IDTs). Each kind of IDT was placed in front of one PC membrane of the two different kinds shown in Figs. 1(a) and 1(b). The different IDTs have been designed to resonantly excite Rayleigh surface acoustic waves at the different frequencies indicated by the dashed lines in Figs. 1(a) and 1(b). All single IDTs were composed by 150 metal-finger pairs with an acoustic aperture of 180 μm, in such a way that they generate a SAW wave front wider than the 150 μm lateral size of the PC devices. More details on sample fabrication are reported in Appendix A. Scanning electron microscopy of a typical device is displayed in Fig. 1(c), showing the IDT and two magnifications of the $R_{PC}$ membrane. By driving the IDT at its resonant frequency, a SAW is generated along [110] through the piezoelectricity of the GaAs layer; the generated SAW impinges on the PC and therein excites mechanical modes that depend on the symmetry of the SAW field.

The mapping of the acoustic fields has been done employing the AAFM technique [29,32]. The AFM detection tip, with resonance frequencies in the kilohertz range, does not directly respond to the GaAs high-frequency SAW vibrations. The technique thus relies on the nonlinear interaction between the tip and the sample surface, which arises from a combination of Coulomb and van der Waals interactions [39]. Such a nonlinearity is well manifested in the dependence of the force acting on the cantilever ($F$) on the tip-to-surface distance $z$ (see Appendix C).

A simplified description of the system approximates the tip as a harmonic oscillator subjected to a time-dependent external forcing $F(z)$ induced by the distance modulation from a Rayleigh SAW, $z = z_0 + z_{SAW}$. Here, $z_{SAW}$ is a harmonic function representing an out-of-plane, standing-wave displacement, i.e., $z_{SAW} = A\cos(\omega_{SAW} t)$. In standard AFMs, the fastest response of the tip is in the hundreds of kilohertz range, limited by the mechanical resonance of the tip-hosting cantilever and the frequency response of the four-quadrant photodetector used to probe the tip deflection. While this is significantly slower than the gigahertz frequency of the SAWs, a displacement contribution appears in the time-averaged, "slow" deflection $\langle d \rangle_T$ [34]:

$$\langle d \rangle_T = \frac{1}{k} F(z) + \underbrace{\frac{1}{k}\left( F''(z)\frac{F'(z)}{F'(z)+k} + \frac{F''(z)}{2} \right) A^2}_{\delta_{SAW}}, \quad (1)$$

where $k$ is the tip cantilever spring constant and all the differentiations are with respect to the $z$ coordinate.

Analyzing the right-hand side of Eq. (1), one notices a first linear term $F(z)/k$, which is responsible for the standard AFM signal yielding the sample topography. Additionally, a nonlinear contribution proportional to a combination of the first and second derivatives of $F$ and the SAW intensity $A^2$ appears. The derivation of Eq. (1) assumed a purely vertical tip-surface distance modulation, which we consider to be the most prominent component detected by AAFM.

Note, however, that this equation can be obtained by considering both traveling and standing acoustic fields. In the latter case, the spatial variations of the average acoustic amplitude enables the mapping of the acoustic wave fronts. In the former, in contrast, traveling phase information is lost and one obtains a signal proportional to the root-mean-square (rms) of the squared amplitude of the acoustic field $A^2$ (see Appendix C).

The generally small signal proportional to $A^2$ can be efficiently detected by employing a lock-in amplifier (LIA). Here, the rf signal driving the SAW is amplitude-modulated at a frequency $f_m$ and the AFM signal component at this frequency is detected by the LIA. The LIA detection can be maximized by choosing a modulation frequency coincident with one of the narrow, higher-order tip cantilever modes. In our experiment, we used a modulation frequency resonant with the 536-kHz mode, which has shown to give the optimal overall results by minimizing the crosstalk between the acoustic displacement and the low-frequency AFM topographic signal. More details on the experimental measurements can be found in Appendix B.

## III. RESULTS

### A. AAFM field mapping

Figures 2(a) and 2(c) compare the directly acquired [i.e., $\langle d \rangle_T$ in Eq. (1)] and the lock-in demodulated AFM deflection signal ($\delta_{SAW}$) for the $R_{PC}$ excited at 1.262 GHz by applying a 20-dBm rf bias to the IDT (the IDT is placed on the left, outside the picture). As expected from Eq. (1), the signal in Fig. 2(a) is essentially proportional to the surface topography: a clear square lattice made of rectangular holes is visible in the center of the map, as well as dust microparticles on the sample surface.

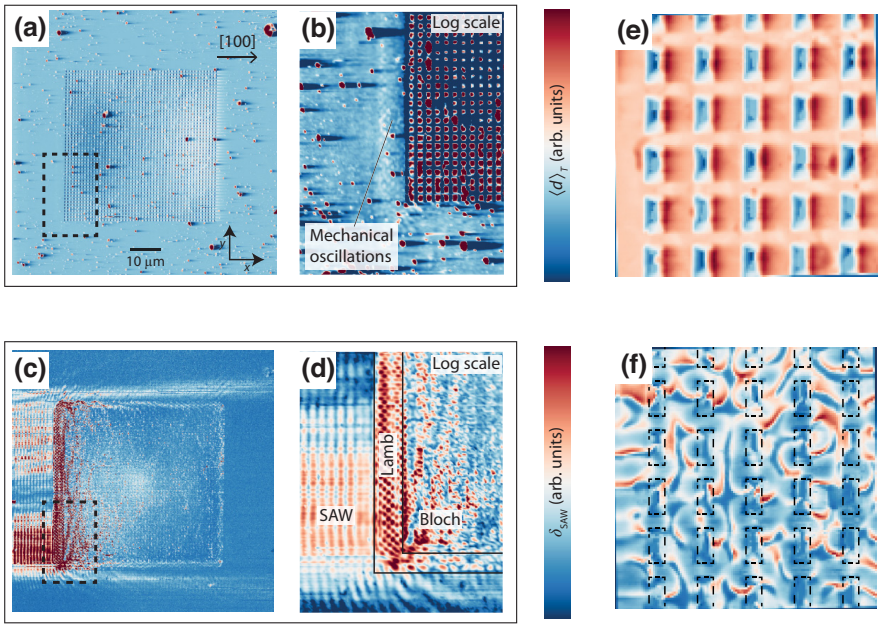


FIG. 2. (a) Direct [i.e., $\langle d \rangle_T$, cf. Eq. (1)] and (b) demodulated ($\delta_{\mathrm{SAW}}$) tip deflection signals detected on the $R_{\mathrm{PC}}$ excited with a 1.262-GHz SAW, both in a linear color scale. (b)–(d) Magnified sections of each map in a logarithmic color scale. (e),(f) Few-unit-cells maps of (e) direct and (f) demodulated signals. In the latter map, the PC holes have been superimposed as dashed rectangles.

Plotting the deflection map in a logarithmic scale allows one to better appreciate the feeble signal originating from mechanical vibrations, as indicated in the magnified view of Fig. 2(b).

By amplifying the $\delta_{\mathrm{SAW}}$ term in Eq. (1) through lock-in demodulation, we obtain the map reported in Fig. 2(c). Here, the incoming SAW wave is clearly visible, as well as several complex features in the patterned region. The magnification of the membrane lower left corner in Fig. 2(d) allows one to easily distinguish three different propagation regions: (i) from the Rayleigh SAW in the bulk, to (ii) a Lamb wave on the unpatterned part of the slab to finally (iii) a Bloch wave inside the phononic crystal patterned in the slab. The mechanical waves can be clearly distinguished, although the high spatial resolution of the AAFM enables us to analyze even smaller features in the devices.

As an example, Fig. 2(e) shows the deflection map of a few phononic crystal unit cells with a resolution of roughly 50 nm. Considering the scanning parameters (i.e., large cantilever from surface distance) and high speed employed in our measurement, the tip can only partly feel the presence of a hole underneath it, resulting in a reduced, but not vanishing, deflection signal in the hole regions. The corresponding displacement square map for the same area is shown in Fig. 2(f). As a visual aid, we have superimposed outlines of the hole shapes on the map. Here, one can observe the complex displacement pattern resulting from the interference of multiple Bloch modes. The intrinsic lateral resolution limit of our technique is the same as in standard AFM and therefore mainly limited by the tip radius. Using conventional tips we expect to achieve a lateral resolution of 5–10 nm, although subnanometer resolution has been demonstrated in an ultrastable system with appropriately sharp tips [40].

### B. SAW scattering

The experimental results of Fig. 2 can be further analyzed to obtain information related to acoustic wave scattering. At first, we focus on the portion of the sample between the IDT and the PC device. Here, the SAW propagates as a quasi-plane-wave with wave vector along the $\hat{x}$ direction and a strong displacement component along $\hat{z}$. To evaluate the average SAW amplitude, we integrated the signal from Fig. 2(c) along $\hat{y}$; the result is displayed in Fig. 3(a). The experimental data can be fitted with a cosine-squared function, $f(x) = A + B\cos(k_0 x)^2$ (red curve). The obtained wave vector is $k_0 = 2.56\ \mu\mathrm{m}^{-1}$, resulting in a SAW phase velocity of $\sim 3094$ m/s, which is compatible with the value of 3022 m/s determined from an elastic model for the sample structure; see, for example, Ref. [41].

Additional information about scattering can be obtained by directly taking the two-dimensional Fourier transform (FT) $\mathcal{F}$ of the entire area between the IDT and the phononic crystal. The reciprocal-space map obtained by operating on Fig. 2(c) is reported in Fig. 3(b). It shows several interesting features: At first, we observe the three bright spots at $k_x = 0$ and $k_x = \pm 0.827 \times 2\pi\ \mu\mathrm{m}^{-1} \approx \pm 2k_0$, respectively. These are expected by considering that the FT of a cosine-squared function produces three $\delta$-functions according to

$$\mathcal{F}[A + B\cos(k_0 x)^2] \propto [\delta(k_x) + \delta(k_x - 2k_0) + \delta(k_x + 2k_0)]. \quad (2)$$

In addition to the three bright spots, Fig. 2(b) also shows two symmetric, slightly deformed ring-shaped structures of radius $k_0$ centered at $[\pm k_0, 0]$. These rings originate from the interference between the incoming SAW with waves non-specularly-reflected at the interface between

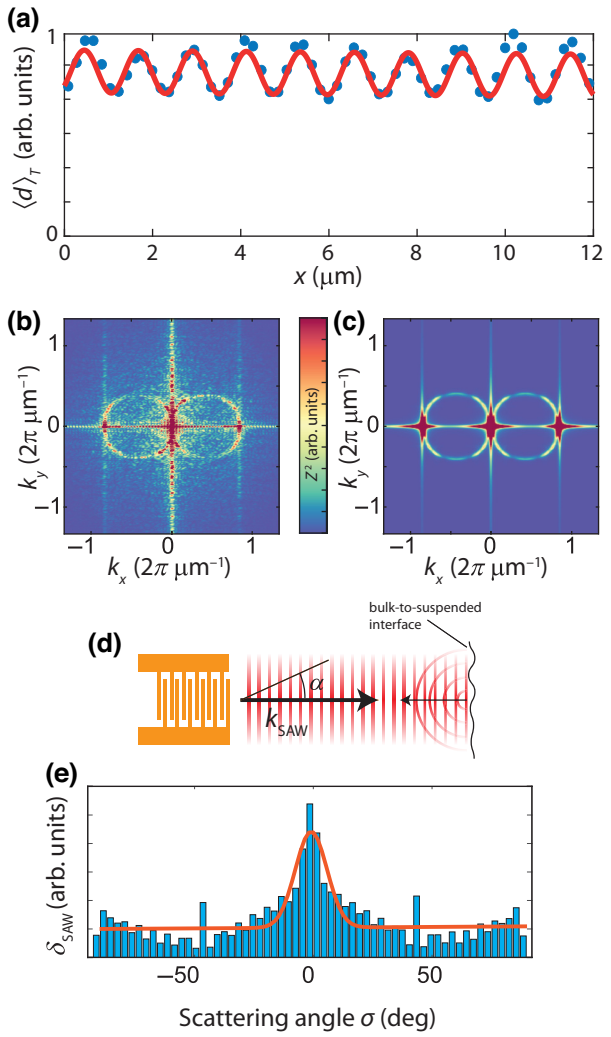


FIG. 3. (a) AAFM signal in the region between the IDT and the PC integrated in the direction perpendicular to the SAW ($y$ direction). (b) Two-dimensional FT of the incoming SAW wave. (c) Two-dimensional FT of a toy model considering a plane wave and an inhomogeneous cylindrical wave. (d) Sketch of the scattering configuration. (e) Angular spread of the wave impinging on the $R_{PC}$ device of Fig. 2. The red line is the best Gaussian fit to the histogram.

the bulk and suspended membrane or scattered at single point defects; see the scheme in Fig. 3(d). As will be demonstrated later, the large mismatch in acoustic impedance at the interface between the bulk and the suspended membrane leads to strong reflections at this interface. In fact, all the features can be qualitatively reproduced by considering a numerical model combining a plane wave (generated SAW) with a weaker cylindrical wave plus an angular-dependent scattering amplitude (the scattered SAWs). Additionally, slightly anisotropic wave propagation has been considered by evaluating the slowness curve in our material heterostructure. The model is described in detail in the Appendix D. The simulated map is reported in Fig. 3(c) and agrees well with the experimental one. Interestingly, the slight deformation of the ring structure that deviates from a perfect circle is well reproduced in the theoretical map and originates from the material anisotropy.

The wave dispersion due to scattering can be more quantitatively estimated from the map of Fig. 3(b). Figure 3(e) is derived from the reciprocal map as a histogram of the FT power as a function of the polar angle, considering $\hat{k}_x$ as the zero-angle direction, as sketched. As can be seen, the histogram has a maximum along the planar SAW propagation direction along $\hat{k}_x$. The maximum then slowly decreases toward a weaker and constant background, which spans from the weak scattering at large angles due to random particles and defects. The histogram of Fig. 3(c) can be fitted with an offset Gaussian function, resulting in an angular spread $\Delta\alpha = 9.6^\circ \pm 2.5^\circ$ for the device under investigation.

A similar analysis was applied to the whole set of devices comprising six $S_{PC}$ and six $R_{PC}$ phononic crystals excited at eight frequencies, ranging from $\sim$ 850 MHz to $\sim$ 1.42 GHz, indicated by the dashed lines in Figs. 1(a) and 1(b). The results are summarized in Figs. 4(a) and 4(b), respectively. The angular spread $\Delta\alpha$ is, to a good approximation, roughly constant for all the investigated devices, with average values of $\sim 10.8^\circ$ and $\sim 11^\circ$ for $S_{PC}$ and $R_{PC}$, respectively. This observation strengthens the hypothesis that the SAW angular spread mainly originates at the bulk-to-suspended interface and it is, therefore, independent of the structure of the PC fabricated within the membrane. In fact, scattering events induced by the PC structure would carry the signatures of its nontrivial energy-band dispersion illustrated in Figs. 1(a) and 1(b).

Looking for a signature in the wave spectral scattering, we used our AAFM characterization to evaluate the reflectivity ($R$) and transmissivity ($T$) of acoustic waves through the PC membrane. An estimation of the reflectivity can be performed by observing that the incoming SAW integrated square displacement in Fig. 3(a) is composed by an oscillating term on a constant background. Our nonlinear detection mechanism averages the signal to a time scale that is orders of magnitude slower than the SAW period. While this is not an issue for standing waves, which have fixed nodes in the spatial coordinates, it produces a constant signal for traveling waves, whose crests travel faster than the detection integration time. Specifically, this would correspond to the squared wave rms amplitude value. These observations suggest that the incoming SAW will likely be composed by a standing wave and a traveling wave components, as expected for a partially reflected wave.

With a simple analytical, one-dimensional model, it is possible to evaluate the SAW reflected amplitude; see Appendix E for more details. This analysis results in a discrete spectral reflectivity $R(f_{IDT})$, evaluated at the

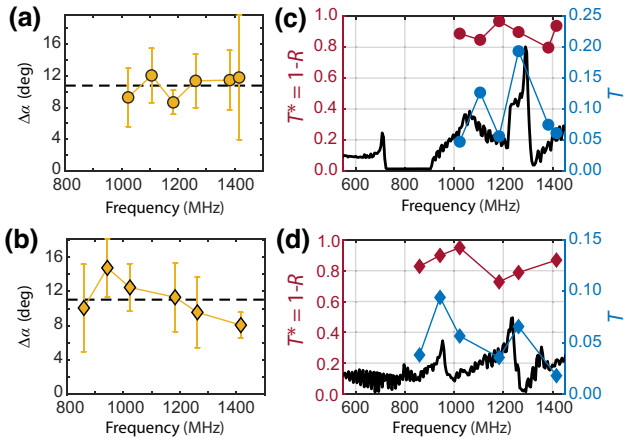


FIG. 4. (a),(b) Angular dispersion of the incoming SAW evaluated from AAFM reciprocal-space maps for (a) $R_{PC}$ and (b) $S_{PC}$. (c),(d) The transmissivity deduced from the standing wave to traveling wave ratio (red) and that directly evaluated (blue) are compared with the crystal density of states (DOS; black) for (c) $R_{PC}$ and (d) $S_{PC}$. The DOS axis starts from zero; the data have been plotted using a common rescaling factor, which puts the maximum of the DOS of panel (c) at $0.8T^*$.

frequency of each IDT for the two sample geometries. To correlate the estimated reflectivity with the PC-induced scattering, we can consider its deduced transmissivity, $T^*(f_{IDT}) = 1 - R(f_{IDT})$, which is a valid approximation if one neglects internal device losses. The deduced transmissivity is plotted in Figs. 4(c) and 4(d), for $R_{PC}$ and $S_{PC}$, respectively. In a rough approximation neglecting the coupling between SAW and PC Bloch modes, the deduced transmissivity can be compared with the integrated PC density of states. As can be seen, $T^*$ correlates poorly with the DOS, once more confirming that the wave reflectivity depends, not on the local PC device, but rather on the bulk-to-membrane interface.

Once the reflectivity has been assessed, the transmissivity can be easily obtained by dividing the integrated total AAFM signal into two planar regions placed before and after the membrane, opportunely modified to consider the (spurious) reflections previously described. The final results for $T$ are added as blue symbols to Figs. 4(c) and 4(d) and show a good correlation with the DOS, for both device geometries. This suggests that the PC can have a strong impact on the propagating SAW and, therefore, can be used for wave manipulation in the gigahertz frequency range employing subwavelength-thick suspended membranes.

### C. Reciprocal-space mapping of phononic crystals

Additional insights into the PC effect on wave manipulation can be obtained by inspecting the AAFM signal within the membrane region. While the experimental maps in real space can be difficult to interpret, their two-dimensional FT can highlight interesting features linked to beam steering and ordinary or negative wave refraction [10,16]. In our device configuration, the SAW impinges on the PC with a set of wave vectors ($|k_{SAW}| = 2\pi f_{IDT}/v_s$, with $v_s$ being the sound velocity) broadened by the angular spread reported in Figs. 3(a) and 3(b). Therefore, one would expect to excite only a certain region of reciprocal space, namely around $\pm k_{SAW}$. Surprisingly, as can be observed by the selected experimental maps in Figs. 5(a) and 5(b), a very wide region of reciprocal space is populated, even in the direction perpendicular to $\hat{k}_{SAW}$. This suggests strong wave scattering within the PC itself, which can either originate from random disorder and/or be governed by the hole symmetry.

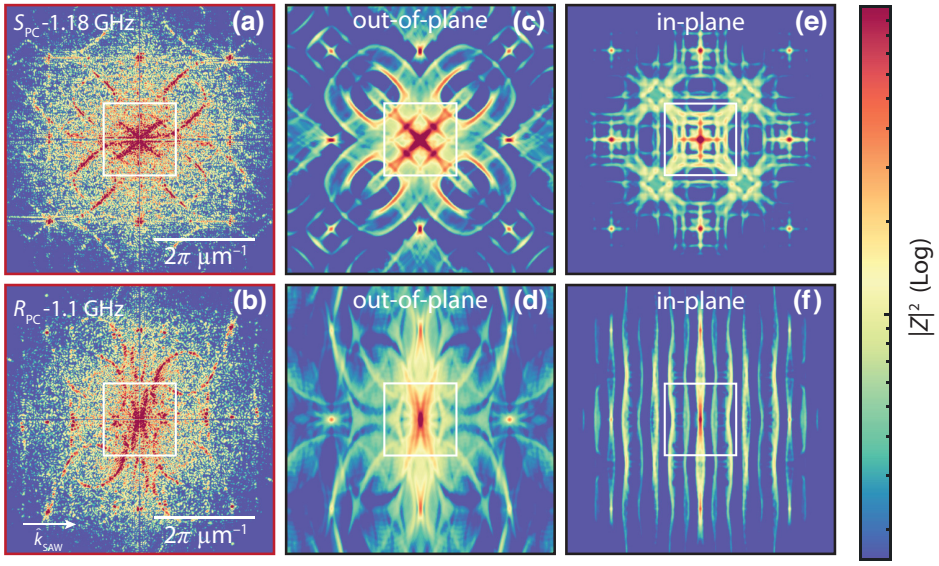


FIG. 5. (a),(b) Experimental reciprocal-space maps of the AAFM signal within the patterned region. Selected maps coming from (a) $S_{PC}$ and (b) $R_{PC}$ have been considered. (c)–(f) Simulated maps for the same PC in a color scale considering the (c),(d) out-of-plane and (e),(f) in-plane displacement components, respectively. The white square represents the edge of the first Brillouin zone.

We note that several detailed features are present in the experimental maps, allowing for an in-depth investigation of the PC eigenmodes as well as of the PC wave manipulation properties. The net effect of the pattern can be evaluated by comparing the experimental reciprocal-space maps with FEM simulations; see Fig. 5. The simulated maps have been evaluated starting from the isofrequency contours in reciprocal space, obtained from a slice of the two-dimensional band-structure simulations. Its self-convolution integral is then equivalent to the FT of the squared signal, which is the quantity measured by the AAFM technique. Moreover, the simulated maps have been colored using a logarithmic weight proportional to the out-of-plane, $\hat{z}$, and in-plane, $\hat{x}$-$\hat{y}$, displacements of the vibrations, more details of which can be found in Ref. [16].

As a general observation, we found excellent agreement between experiments and out-of-plane simulations, with fine features clearly present in both maps. Conversely, we do not see any relevant correlation between experiments and in-plane simulations, suggesting that, in our measurement configuration, the AAFM is mostly sensitive to the out-of-plane mechanical vibrations. Indeed, the AAFM can be tailored for an enhanced sensitivity in the detection of planar modes, especially when in proximity to a hole [42], although this feature is not relevant in this experiment. The distortions and different amplitudes of some of the experimental features with respect to the simulated ones can be imputed to the nonflatness of the membranes, which can be slightly buckled due to the softness of the GaAs material.

Another interesting observation can be made by considering the general shape of the reciprocal-space maps, which are more isotropic for $S_{\mathrm{PC}}$ [Figs. 5(a) and 5(c)], while being more elongated for $R_{\mathrm{PC}}$ [Figs. 5(b) and 5(d)], respectively. This is linked to the pattern symmetry, which enhances or suppresses wave scattering in certain directions according to the energy-momentum dispersion of the Bloch modes. A more quantitative analysis of the isotropy of the reciprocal-space maps has been performed by comparing the distribution of modes along the $\hat{k}_x$ and $\hat{k}_y$ directions. It has been found that $S_{\mathrm{PC}}$ shows very similar distributions, with a $\Delta k_x$ to $\Delta k_y$ average ratio of $0.96 \pm 0.08$; conversely, $R_{\mathrm{PC}}$ shows an average ratio of $0.72 \pm 0.08$, with a broader distribution $\Delta k_y$ given by the reduced symmetry of its unit cell. Details on the reciprocal-space isotropy analysis are available in Appendix F.

The results illustrated here show that, on top of an inhomogeneous scattering background due to pervasively present device nonidealities, a strong phonon scattering channel is governed by the local band structure, which ultimately determines the density of available states in the system. In analogy with transport in optical systems, one can imagine several ways to manipulate elastic waves by DOS engineering. As an example, one can use $S_{\mathrm{PC}}$ as complex spectral filters, while $R_{\mathrm{PC}}$ grants an additional spatially dependent effect, stopping waves propagating along a certain direction while allowing the transmission of waves coming, for example, along the perpendicular direction. This and more complex features can be introduced to create complex nodes in elastic networks, which can act as manipulators for microwave-based telecom technology.

## IV. CONCLUSIONS

In this paper, we have introduced an AFM-based technique for the detailed characterization of gigahertz phononic crystal membrane devices. The high spatial resolution of this technique along with its rapid scanning times make it perfectly suited for investigating mechanical devices operating at gigahertz frequencies and above. Elastic photonic crystals and mechanical metasurfaces supporting high-frequency waves can find a wide application in the next-generation telecommunication technologies, where electromagnetic waves can be processed by coupling them to mechanical channels, as routinely done with SAW filters in mobile device technology. The design flexibility of periodic devices opens the way for complex wave-based functionalities, possibly enabling the emergence of 6G technologies, where the increased carrier wave frequency could be accompanied by parallel manipulation and multiplexing based on spatial, spectral, and/or polarization features.

As a proof of concept, here we have studied with the AAFM technique a set of phononic crystals with different symmetries and operating at $\sim 1$ GHz frequency. By employing reciprocal-space analysis, we have quantified the role of inhomogeneous and homogeneous scattering, the latter showing features connected with the crystal symmetry itself. The simple geometrical features employed here can be useful for realizing complex spectral filters which are additionally dependent on the elastic wave vectors.

## ACKNOWLEDGMENTS

We acknowledge Dr. Nazim Ashurbekov for a critical reading of the manuscript. The Alexander von Humboldt Foundation is gratefully acknowledged for funding this research through the Experienced Researcher Fellowship program.

## APPENDIX A: SAMPLE FABRICATION

The fabrication of the devices under investigation starts by defining the interdigital transducers on the top surface of a 500/220 nm $Al_{0.5}Ga_{0.5}As$/GaAs heterostructure which had been deposited on an undoped GaAs wafer. This has been done by creating a poly(methyl methacrylate) mask of the single finger electrodes via electron-beam lithography, followed by 50-nm thermal evaporation of Au and lift-off. A second aligned lithography has been used to define

the thicker (5/80 nm Cr/Au) IDT side contacts and bonding pads. The different metal thicknesses were necessary in order to reduce the mass loading on the generated surface acoustic wave and, consequently, the wave reflection within the IDT, while a thicker metal layer was used to ease the wire bonding operations.

In front of each IDT, we defined a membrane with a phononic square lattice made with either square or rectangular holes, respectively. To this end, an AR-P 6200 resist mask (Allresist GmbH) comprising 150 × 150 repetitions of the unit cell for each geometry [i.e., with square ($S_{PC}$) or rectangular ($R_{PC}$) holes] was defined via electron-beam lithography, followed by chlorine-based inductively coupled reactive ion etching. A final HF wet etching has been used to remove the 500-nm $Al_{0.5}Ga_{0.5}As$ sacrificial layer underneath the GaAs slab, completely suspending the patterned region and forming membranes with side $\sim 150$ μm. More details on sample fabrication can be found elsewhere [16].

## APPENDIX B: EXPERIMENTAL SETUP AND IDT CHARACTERIZATION

Our experimental setup is sketched in Fig. 6(a). The core of the system is represented by a commercial AFM probe (Nanosurf Nanoflex): conceptually, the cantilever deflection is measured using a lever-arm approach with four-quadrant detection. The direct deflection signal was used to evaluate $\langle d \rangle_T$, which is mainly proportional to the topography of the investigated surface. The direct deflection signal was simultaneously fed as the input of a lock-in amplifier, whose reference was used to amplitude-modulate a radio-frequency source. The source signal, composed of a fast frequency component (in the range of gigahertz) and a slow modulated component (in the range of hundreds of kilohertz), was used to bias an IDT which excited the SAW on the device under investigation.

In this configuration, the output of the lock-in amplifier directly gives the squared amplitude of the acoustic wave $\delta_{SAW}$. The different components in the experiment set the maximum operating speed of the AAFM, including the cantilever eigenmode frequencies and four-quadrant detection speed. Most of the experimental noise comes from environmental factors but can be strongly reduced by using lock-in amplification. In this regard, the lock-in time constant has to be compatible with the probe scanning parameters; low scanning frequencies allow more signal integration and produce higher signal-to-noise ratio, to the detriment of fast acquisition.

A preliminary characterization of the device has been performed by evaluating the one-port $S$ parameter for every IDT. The measurements were performed with uncalibrated cables, and their main goal was to assess the resonating frequency. A more quantitative estimation of the generated SAW has been reported for an identical set

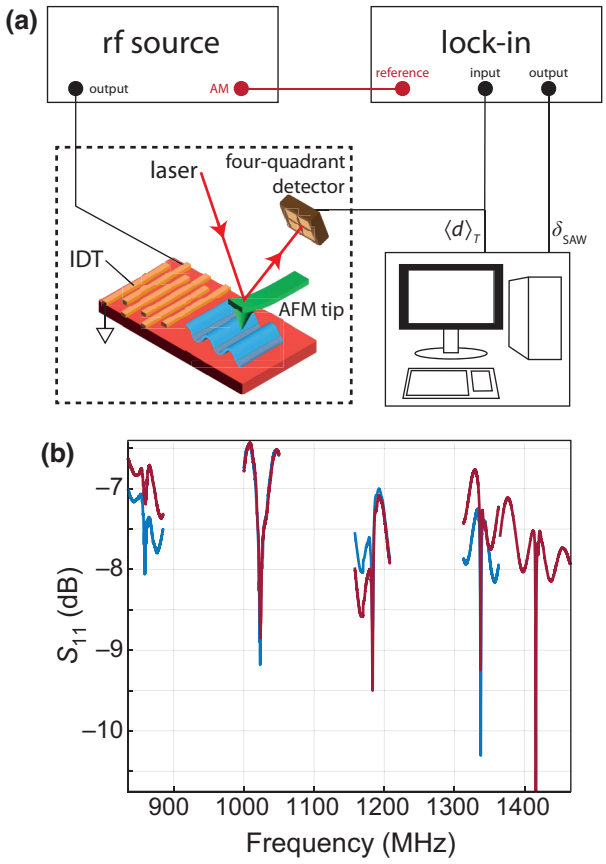


FIG. 6. (a) Sketch of the experimental setup. (b) The $S_{11}$ parameter of typical IDTs facing the $S_{PC}$ (red) and $R_{PC}$ (blue).

of devices elsewhere [16]. Figure 6 reports the typical $S_{11}$ parameter obtained for the IDTs exciting the $S_{PC}$ (red) and those exciting the $R_{PC}$ (blue). As can be seen, nominally identical IDTs resonate at the same frequency, validating the good reproducibility of the fabricated devices.

## APPENDIX C: BASICS OF ACOUSTIC FORCE MICROSCOPY

Atomic acoustic force microscopy is a powerful technique for the characterization of elastic waves on-chip. To understand the physical meaning of the signal obtained from AAFM, we can follow the analysis of Hellemann *et al.* [34]. Let us assume that an atomic force microscope tip approaches the sample surface from the vertical direction $\hat{z}$. At any given point, the base on the cantilever supporting the tip will be at a coordinate $z_0 + d$, with $z_0$ being the tip-to-surface distance and $d$ the cantilever deflection [see Fig. 7(a)]. The deflection is given by the interaction between the tip and the sample surface, which can mainly be summarized by considering the Coulomb repulsive and van der Waals attractive forces [see Fig. 7(d)].

In our operating mode, the cantilever vertical position is set to be maintained at a certain value of the force acting

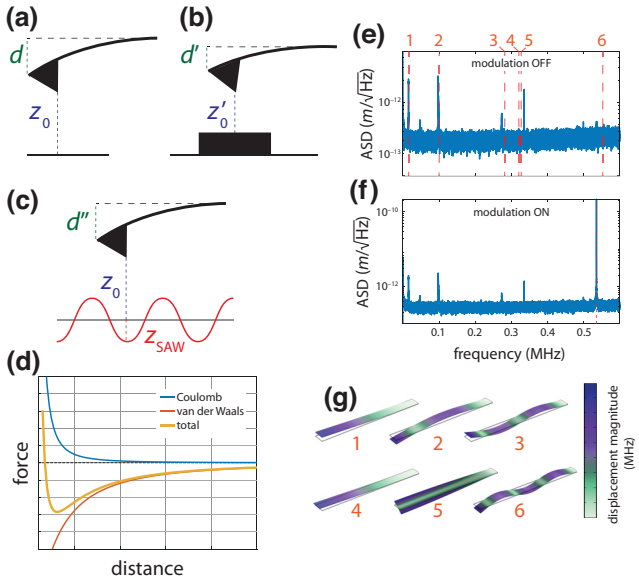


FIG. 7. (a)–(c) Sketches of the cantilever tip position: (a),(b) in standard AFM operation, and (c) in the presence of a mechanical SAW wave. (d) Typical force-distance curve in an AFM system. (e),(f) Mechanical spectrum of the cantilever tip as measured by the AFM photodetector with the SAW modulation (e) off and (f) on. The vertical dashed lines indicate the first six cantilever mode frequencies determined by FEM simulations, whose displacement patterns are plotted in panel (g).

on the tip, which only depends on $z_0$. If the tip is scanned along the sample surface, hills and valleys translate into a new equilibrium position $z_0' + d'$ [see Fig. 7(b)], allowing one to obtain the tip-to-sample distance by measuring the cantilever deflection with a lever-arm laser and a multiquadrant detector. If we add a vertically displaced wave to the system, we need to consider a further displacement, $z_{\mathrm{SAW}}$, which in our case can be described by a simple wave function, $z_{\mathrm{SAW}} = A\cos(\omega_{\mathrm{SAW}}t)$ [see Fig. 7(c)].

Approximating the AFM cantilever tip as a harmonic oscillator with external forcing, we can consider:

$$m\ddot{z} + m\Omega^2 z = F[z_0 + d + A\cos(\omega_{\mathrm{SAW}}t)], \tag{C1}$$

where $m$ is the effective oscillator mass and $F(z)$ is the force-distance curve, qualitatively sketched in Fig. 7(d). We can start by expanding the force term around the small SAW amplitude $A$:

$$\begin{aligned} F \to\ & F(z_0 + d) + F'(z_0 + d)A\cos(\omega_{\mathrm{SAW}}t) \\ & + F''(z_0 + d)\tfrac{1}{2}A^2\cos^2(\omega_{\mathrm{SAW}}t), \end{aligned} \tag{C2}$$

and writing the cantilever deflection as the sum of slow, $D(t)$, and fast, $\delta(t)$, contributions, the former being essentially given by a long-time average of $d(t)$, $D(t) = \langle d(t)\rangle_T$. With some algebra and further expanding some force terms at the first order in $\delta$, Eq. (C1) can be split into two equations for the slow and fast components:

$$\begin{aligned} m(\ddot{D} + \Omega^2 D) =\ & F(z_0 + D) + \big\langle F'(z_0 + D)A\cos(\omega_{\mathrm{SAW}}t) \\ & + F''(z_0 + D)\delta A\cos(\omega_{\mathrm{SAW}}t) \\ & + F''(z_0 + D)\tfrac{1}{2}A^2\cos^2(\omega_{\mathrm{SAW}}t)\big\rangle_T, \\ m(\ddot{\delta} + \Omega^2\delta) =\ & F(z_0 + D)\delta + F'(z_0 + D)A\cos(\omega_{\mathrm{SAW}}t) \\ & + F''(z_0 + D)\delta A\cos(\omega_{\mathrm{SAW}}t) \\ & + F''(z_0 + D)\tfrac{1}{2}A^2\cos^2(\omega_{\mathrm{SAW}}t), \end{aligned} \tag{C3}$$

where the last terms of the slow deflection equation are averaged for a time $T \gg 2\pi/\omega_{\mathrm{SAW}}$.

To solve the system of equations (C3), we can start by assuming that $\delta(t)$ is a harmonic function, i.e., $\ddot{\delta} = -\omega_{\mathrm{SAW}}^2\delta$, and that its oscillating frequency is very large with respect to the typical frequencies of the cantilever-tip harmonic oscillator, $\Omega^2\delta \ll \ddot{\delta}$. Under these assumptions, we can find an expression for $\delta$:

$$\begin{aligned} \delta = & \left[F' + F''\frac{A}{2}\right]A\cos(\omega_{\mathrm{SAW}}t) \\ & \times \frac{1}{-m\omega_{\mathrm{SAW}}^2 + [F' + F''A\cos(\omega_{\mathrm{SAW}}t)]}, \end{aligned} \tag{C4}$$

where we have simplified the notation by dropping the explicit dependence of $F$ and its derivatives on $z_0 + D$. Manipulating the slow deflection equation in Eq. (C3) by explicitly performing the time average, we obtain

$$\begin{aligned} & \langle F'(z_0 + D)A\cos(\omega_{\mathrm{SAW}}t)\rangle_T = 0, \\ & \langle F''(z_0 + D)\delta A\cos(\omega_{\mathrm{SAW}}t)\rangle_T \\ & \quad = F''(z_0 + D)A\langle\delta\cos(\omega_{\mathrm{SAW}}t)\rangle_T, \\ & \langle F''(z_0 + D)\tfrac{1}{2}A^2\cos^2(\omega_{\mathrm{SAW}}t)\rangle_T = F''(z_0 + D)\tfrac{1}{4}A^2. \end{aligned} \tag{C5}$$

Finally, using Eq. (C4) of the main text and keeping all terms up to $\mathcal{O}(A^2)$, we obtain the following equation for the slow deflection $D$:

$$m(\ddot{D} + \Omega^2 D) = F + \frac{F'F''}{F' + m\omega^2}\frac{A^2}{2} + F''\frac{A^2}{4}. \tag{C6}$$

Its steady-state solution is Eq. (1) in the main text, also reported (in slightly different form) in the following for convenience:

$$\langle d\rangle_T = \frac{1}{k}\left[F + \left(F''\frac{F'}{F' + k} + \frac{F''}{2}\right)A^2\right], \tag{C7}$$

where $k$ is the cantilever spring constant. The expression for the slow deflection has a first term linear in the

force-distance curve and giving the sample topography as in standard AFM technique. The second term, proportional to the nonlinearity of the force-distance curve times the square displacement of the SAW, returns the square mechanical displacement. In practical situations, this is orders of magnitude smaller than the topography contribution, making its detection challenging. The two terms can be better discriminated by adding a modulation frequency to the mechanical waves under investigation and employing lock-in (LI) detection.

An interesting feature is to exploit the cantilever tip resonance frequencies to enhance the LI detection. Figure 7(e) reports a cantilever mechanical spectrum as directly measured within the AFM, showing several resonances up to a maximum frequency mainly determined by the detector bandwidth. The cantilever we used in our experiment had a spring constant of 0.2 N/m (with a 15% maximum difference for different cantilevers belonging to the same set), determining a fundamental mode frequency of about 12 kHz. Employing FEM simulations, we can simulate the measured cantilever modes, obtaining a good match with the experiment.

Most of the modes have a strong out-of-plane vibration, as shown in Fig. 7(g), where the normalized mode deformation is plotted in a color scale indicating the magnitude of the total mechanical displacement. The motion of mode 4 is mainly planar and, therefore, it weakly couples with the AFM lever-arm detection scheme, thus remaining invisible in the cantilever spectrum. Since the cantilever is operating in the static mode, in principle, the mechanical modulation can be chosen to resonate with any of these frequencies. We observed in the experiment that the lowest-frequency modes give a strong mixing of topography and displacement signal, given by the fact that they partially overlap with the typical frequencies of tip-scanning operation, usually around a few kilohertz. The selected modulation for our experiment was resonating with the 536 kHz cantilever mode: this choice gives a strong LI signal enhancement [see Fig. 7(f)] with minimal overlap with the topographic signal.

## APPENDIX D: SAW SCATTERING

The reciprocal-space map of Fig. 3(b) in the main text can be reproduced using a simple toy model which results in the theoretical map of Fig. 3(c). Such a toy model considers that the SAW that originated from the IDT propagates mostly as a plane wave, with wave vector $k_0$ determined by the IDT spacing. Its spatial dependence can be easily represented by a normalized function $f_{\mathrm{pw}}(x,y) = e^{-k_0 x}$ [see Fig. 8(a)]. The effect of scattering due to defects, nonflat interfaces, etc. can be included by assuming that the scattering transforms the plane wave into a spherical one with an angle-dependent amplitude and wave vector [see Fig. 8(b)]. The varying amplitude has been described using a Gaussian function centered on the unperturbed wave direction and with an angular width as estimated by the experimental map of Fig. 3(c) in the main text.

The Gaussian function has been plotted in Fig. 8(d). Such a function successfully describes the scattering contribution from the non-perfectly-flat bulk-membrane interface, which is likely to produce small angular dispersion around the unperturbed wave direction, and the role of small scattering centers, which produce the constant angular background contribution. Moreover, the anisotropic material velocities in different directions have been included, starting from the slowness profile of Fig. 8(e), determined from an elastic model for the sample structure; see, for example, Ref. [41]. The introduction of anisotropies results in the noncircular wave fronts of Fig. 8(b) and ultimately in the slight deformation of the ring features in Fig. 3(c) in the main text. The sum of the unperturbed plane wave and the weakest scattering wave has been reported in Fig. 8(c): its two-dimensional Fourier transform produces the map of Fig. 3(c), which is in good agreement with the experimental results of Fig. 3(b).

## APPENDIX E: STANDING VERSUS TRAVELING WAVES—ANALYTICAL MODEL

By evaluating the signal of the SAW impinging on the PC devices, it is possible to obtain an estimate of its reflected amplitude. This has been done by employing a simple, one-dimensional model. Let us start by considering two plane waves with respective amplitudes $W_1$ and $W_2$, propagating with opposite wave vectors along the $\hat{x}$ direction:

$$W_1 e^{i(kx-\omega t)} + W_2 e^{i(-kx-\omega t)} = e^{-i\omega t}[(W_1 + W_2)\cos(kx) + i(W_1 - W_2)\sin(kx)]. \tag{E1}$$

Assuming an incident wave of amplitude $W_1$, the reflectivity coefficient will be given by $r = W_2/W_1$. It is easy to see that, for $r = 1$, the total wave is a standing wave, with nodes defined by $\cos(kx) = 0$.

On the other hand, if $r = 0$, the total wave is a traveling wave with amplitude $W_1$. In every other case, the total wave has a mixed nature between standing and traveling waves. With simple algebra and with the further normalization of $W_1 = 1$ (giving $r \equiv R$), measuring the waves with the AAFM would return the time-averaged signal $\langle Z^2 \rangle_T$, which reads as

$$\langle Z^2 \rangle_T = |(1 + R)\cos(kx) + i(1 - R)\sin(kx)|^2. \tag{E2}$$

The results of Eq. (E2) for varying values of reflectivity have been reported in Fig. 9(a). As can be seen, the function consists of a combination with different weights of a

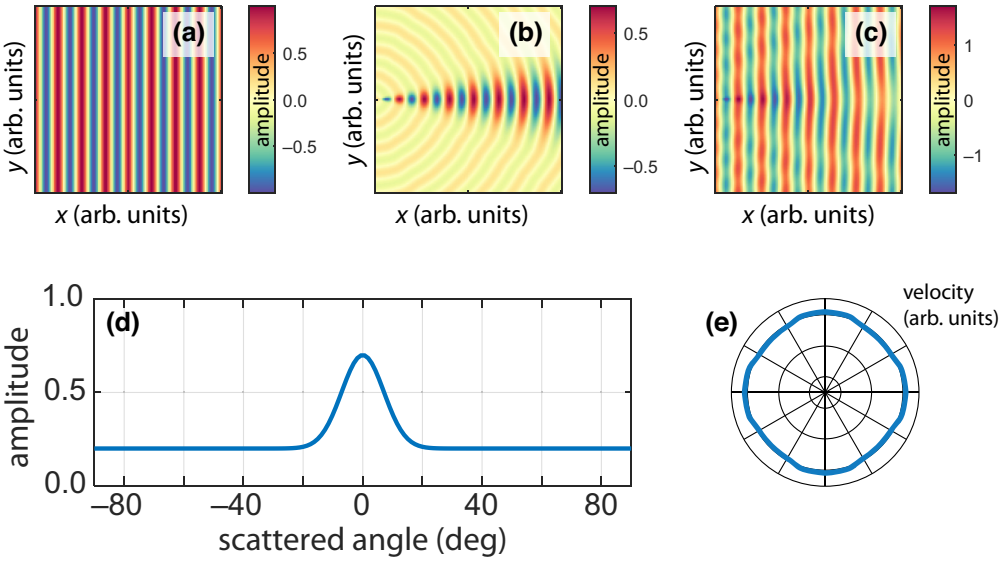


FIG. 8. Map of a plane wave (a), an inhomogeneous circular wave (b) and their sum (c). The inhomogeneous circular wave amplitude can be represented by an offset Gaussian in polar coordinates (d).

constant offset (originating from the traveling-wave contribution) and with an oscillating component with fixed nodes (arising from the standing-wave contribution).

By evaluating the function in Eq. (E2), amplitude versus offset ratio, one can easily deduce the wave reflectivity. The explicit numerical relation between $R$ and wave parameters has been reported in Fig. 9(b). The function described here can be used to obtain the wave reflectivity, once the wave amplitude and offset have been obtained by means of AAFM in our experiment. This has been applied to each incoming SAW in every device, finally obtaining the results reported in Fig. 4 in the main text.

## APPENDIX F: FURTHER INSIGHTS INTO RECIPROCAL-SPACE MAPS

A further interesting analysis of the PC arises by observing that the maps of Fig. 5 of the main text clearly show a different distribution of modes for the two classes of phononic crystals investigated here [i.e., lattices with square ($S_{PC}$) or rectangular ($R_{PC}$) holes]. Applying a threshold filter on the experimental data, we can evaluate more quantitatively the number of reciprocal-space vectors excited along the $\hat{k}_x$ and $\hat{k}_y$ directions, respectively.

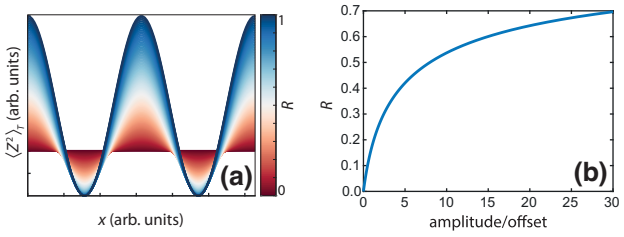


FIG. 9. (a) Time-averaged, squared amplitude of a plane wave impinging on a layer with varying reflectivity. The constant signal of the pure traveling wave gives way to the crest of a pure standing waves, with zero signal nodes. (b) Reflectivity as a function of the ratio of wave amplitude and offset.

Figure 10 reports this kind of analysis for $R_{PC}$ excited at 1.1 GHz, whose false-color reciprocal-space map in a linear scale is shown in Fig. 5(b) in the main text. The filter applied considered the values between $10M$ and $20M$, with $M$ being the reciprocal-space map mean value. The filtered $k$-points are reported in Fig. 10(a) along with their histograms for the $\hat{k}_x$ and $\hat{k}_y$ directions. The distributions are not smooth, given the complex landscape of mechanical modes available at any frequency, including those with varying coupling with the SAW as well as diverse out-of-plane displacement component and therefore different AAFM sensitivities. As a first-order approximation, the distributions can be fitted with Gaussian functions; the curve widths $\sigma_x$ and $\sigma_y$ return a good estimate of preferential excitation along $\hat{x}$ and $\hat{y}$ directions, respectively. For example, the two distributions in Fig. 10 have quite different widths, as one would expect considering the elongated rectangular holes in the device pattern.

A similar analysis has been performed on the whole set of devices under investigation. The frequency dependence of the ratio of the Gaussian widths, $\Delta k_x/\Delta k_y$, is shown in Fig. 10(b) for each of the PC geometries. As qualitatively observed before, most $S_{PC}$ devices show an isotropic spread of reciprocal-space vectors, with an average distribution of $\Delta k_x/\Delta k_y = 0.96 \pm 0.08$, as shown by the red diamonds in Fig. 10(b). Conversely, the reciprocal-space distribution of $R_{PC}$-type devices is more accentuated in the $\hat{k}_y$ direction (cf. blue circles in Fig. 10(b)). This holds an average ratio of Gaussian widths of $0.72 \pm 0.08$, although interestingly the lower-frequency modes show a more

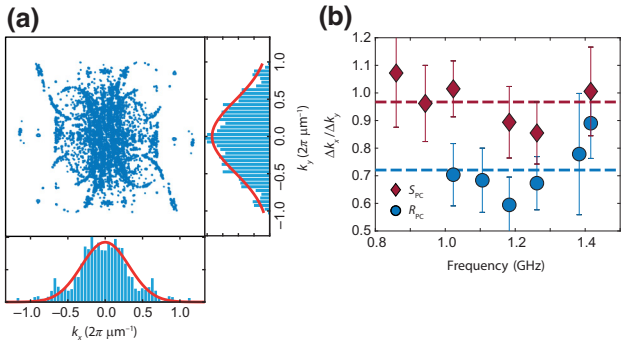


FIG. 10. (a) Filtered reciprocal-space map. The unfiltered map is displayed in Fig. 5(b) of the main text. The FT-power distribution histograms in $\hat{k}_x$ and $\hat{k}_y$ along with their best fits are displayed in the respective panels. (b) Ratio of the distribution widths along perpendicular directions for all devices in the two PC sets.

profound asymmetry than the higher-frequency ones, as one could qualitatively expect by observing the band structure of Fig. 1(b) of the main text.


[1] L. Rayleigh, On waves propagated along the plane surface of an elastic solid, Proc. London Math. Soc. **s1-17**, 4 (1885).

[2] W. Reza Ali and M. Prasad, Piezoelectric MEMS based acoustic sensors: A review, Sens. Actuators A: Phys. **301**, 111756 (2020).

[3] J. Devkota, P. R. Ohodnicki, and D. W. Greve, SAW sensors for chemical vapors and gases, Sensors **17**, 801 (2017).

[4] K. Länge, B. E. Rapp, and M. Rapp, Surface acoustic wave biosensors: A review, Anal. Bioanal. Chem. **391**, 1509 (2008).

[5] D. Morgan, *Surface Acoustic Wave Filters: With Applications to Electronic Communications and Signal Processing* (Academic Press, Oxford, 2010).

[6] R. P. Bernardo, SAW voltage-controlled oscillators (application note), Microw. J. (Int. Ed) **45**, 166 (2002).

[7] K.-Y. Hashimoto, *Surface Acoustic Wave Devices in Telecommunications* (Springer, Berlin, Heidelberg, 2000).

[8] P. Delsing, A. N. Cleland, M. J. Schuetz, J. Knörzer, G. Giedke, J. I. Cirac, K. Srinivasan, M. Wu, K. C. Balram, and C. Bäuerle *et al.*, The 2019 surface acoustic waves roadmap, J. Phys. D: Appl. Phys. **52**, 353001 (2019).

[9] M. Xu, W. S. Harley, Z. Ma, P. V. S. Lee, and D. J. Collins, Sound-speed modifying acoustic metasurfaces for acoustic holography, Adv. Mater. **35**, 2208002 (2023).

[10] H. He, C. Qiu, L. Ye, X. Cai, X. Fan, M. Ke, F. Zhang, and Z. Liu, Topological negative refraction of surface acoustic waves in a Weyl phononic crystal, Nature **560**, 61 (2018).

[11] J. Cha, K. Kim, and C. Daraio, Experimental realization of on-chip topological nanoelectromechanical metamaterials, Nature **564**, 229 (2018).

[12] X. Zhang, M. Xiao, Y. Cheng, M.-H. Lu, and J. Christensen, Topological sound, Commun. Phys. **1**, 97 (2018).

[13] L. Luo, H.-X. Wang, Z.-K. Lin, B. Jiang, Y. Wu, F. Li, and J. J.-H., Observation of a phononic higher-order Weyl semimetal, Nat. Mater. **20**, 794 (2021).

[14] L. Shao, W. Mao, S. Maity, N. Sinclair, Y. Hu., Y. Lang, and M. Lončar, Non-reciprocal transmission of microwave acoustic waves in nonlinear parity–time symmetric resonators, Nat. Electron. **3**, 267 (2020).

[15] F. Gao, S. Benchabane, A. Bermak, S. Dong, and A. Khelif, On-chip tightly confined guiding and splitting of surface acoustic waves using line defects in phononic crystals, Adv. Funct. Mat. **33**, 2213625 (2023).

[16] S. Zanotto, G. Biasiol, P. Santos, and A. Pitanti, Metamaterial-enabled asymmetric negative refraction of GHz mechanical waves, Nat. Commun. **13**, 5939 (2019).

[17] M. M. De Lima, Jr. and P. V. Santos, Modulation of photonic structures by surface acoustic waves, Rep. Prog. Phys. **68**, 7 (2005).

[18] A. Pitanti, T. Makkonen, M. F. Colombano, S. Zanotto, L. Vicarelli, M. Cecchini, A. Griol, D. Navarro-Urrios, C. Sotomayor-Torres, and A. Martinez *et al.*, High-frequency mechanical excitation of a silicon nanostring with piezoelectric aluminum nitride layers, Phys. Rev. Appl. **14**, 014054 (2020).

[19] M. Forsch, R. Stockill, A. Wallucks, I. Marinković, C. Gärtner, R. A. Norte, F. van Otten, A. Fiore, K. Srinivasan, and S. Gröblacher, Microwave-to-optics conversion using a mechanical oscillator in its quantum ground state, Nat. Phys. **16**, 69 (2019).

[20] D. Navarro-Urrios, M. F. Colombano, G. Arregui, G. Madiot, A. Pitanti, A. Griol, T. Makkonen, J. Ahopelto, C. M. Sotomayor-Torres, and A. Martínez, Room-temperature silicon platform for GHz-frequency nanoelectro-optomechanical systems, ACS Phot. **9**, 413 (2022).

[21] A. Khelif, A. Choujaa, B. Djafari-Rouhani, M. Wilm, S. Ballandras, and V. Laude, Trapping and guiding of acoustic waves by defect modes in a full-band-gap ultrasonic crystal, Phys. Rev. B **68**, 214301 (2003).

[22] K. Fang, M. H. Matheny, X. Luan, and O. Painter, Optical transduction and routing of microwave phonons in cavity-optomechanical circuits, Nat. Phot. **10**, 489 (2016).

[23] K. Kokkonnen and M. Kaivola, Scattering of surface acoustic waves by a phononic crystal revealed by heterodyne interferometry, Appl. Phys. Lett. **91**, 083517 (2007).

[24] D. M. Profunser, E. Muramoto, O. Matsuda, O. B. Wright, and U. Lang, Dynamic visualization of surface acoustic waves on a two-dimensional phononic crystal, Phys. Rev. B **80**, 014301 (2009).

[25] Y. Achaoui, A. Khelif, S. Benchabane, L. Robert, and V. Laude, Experimental observation of locally-resonant and Bragg band gaps for surface guided waves in a phononic crystal of pillars, Phys. Rev. B **83**, 104201 (2011).

[26] M. Kurosu, D. Hatanaka, K. Onomitsu, and H. Yamaguchi, On-chip temporal focusing of elastic waves in a phononic crystal waveguide, Nat. Comm. **9**, 1331 (2018).

[27] G. Carlotti, Elastic characterization of transparent and opaque films, multilayers and acoustic resonators by surface Brillouin scattering: A review, Appl. Sci. **8**, 124 (2018).

[28] O. Florez, G. Arregui, M. Albrechtsen, R. C. Ng, J. Gomis-Bresco, S. Stobbe, C. M. Sotomayor-Torres, and

P. D. García, Engineering nanoscale hypersonic phonon transport, Nat. Nanotechnol. **17**, 947 (2022).
[29] U. Rabe and W. Arnold, Acoustic microscopy by atomic force microscopy, Appl. Phys. Lett. **64**, 1493 (1994).
[30] E. Chilla, T. Hesjedal, and H. J. Fröhlich, Nanoscale determination of phase velocity by scanning acoustic force microscopy, Phys. Rev. B **55**, 15852 (1997).
[31] F. Kubat, W. Ruile, T. Hesjedal, J. Stotz, U. Rosler, and L. M. Reindl, Calculation and experimental verification of the acoustic stress at GHz frequencies in SAW resonators, IEEE T. Ultrason. Ferr. **51**, 1437 (2004).
[32] T. Hesjedal, Surface acoustic wave-assisted scanning probe microscopy—A summary, Rep. Prog. Phys. **73**, 016102 (2010).
[33] S. Hu, C. Su, and W. Arnold, Imaging of subsurface structures using atomic force acoustic microscopy at GHz frequencies, J. Appl. Phys. **109**, 084324 (2011).
[34] J. Hellemann, F. Müller, M. Msall, P. V. Santos, and S. Ludwig, Determining amplitudes of standing surface acoustic waves via atomic force microscopy, Phys. Rev. Appl. **17**, 044024 (2022).
[35] K. Fricke, Piezoelectric properties of GaAs for application in stress transducers, J. Appl. Phys. **70**, 914 (1991).
[36] S. Zanotto, G. Mazzamuto, F. Riboli, G. Biasiol, G. C. La Rocca, A. Tredicucci, and A. Pitanti, Photonic bands, superchirality, and inverse design of a chiral minimal metasurface, Nanophotonics **8**, 2291 (2019).
[37] S. Zanotto, A. Tredicucci, D. Navarro-Urrios, M. Cecchini, G. Biasiol, D. Mencarelli, L. Pierantoni, and A. Pitanti, Optomechanics of chiral dielectric metasurfaces, Adv. Opt. Mater. **8**, 1901507 (2020).
[38] G. Conte, L. Vicarelli, S. Zanotto, and A. Pitanti, Mechanical mode engineering with orthotropic metamaterial membranes, Adv. Mater. Technol. **7**, 2200337 (2022).
[39] H. J. Sharahi, M. Janmaleki, L. Tetard, S. Kim, H. Sadeghian, and G. J. Verbiest, Acoustic subsurface-atomic force microscopy: Three-dimensional imaging at the nanoscale, J. Appl. Phys. **129**, 030901 (2021).
[40] F. J. Giessibl, Advances in atomic force microscopy, Rev. Mod. Phys. **75**, 949 (2003).
[41] M. M. de Lima and P. V. Santos, Modulation of photonic structures by surface acoustic waves, Rep. Prog. Phys. **68**, 1639 (2005).
[42] G. Behme and T. Hesjedal, Influence of surface acoustic waves on lateral forces in scanning force microscopies, J. Appl. Phys. **89**, 4850 (2001).